Sedimentary structure derived from multi-mode ambient noise tomography with dense OBS network at the Japan Trench

Lina Yamaya[1], Kimihiro Mochizuki[1], Takeshi Akuhara[1], Kiwamu Nishida[1]

[1]Earthquake Research Institute, University of Tokyo, Tokyo, 113-0023, Japan

Correspondence to: Lina Yamaya (lina@eri.u-tokyo.ac.jp)

Abstract. We derive the 3-D S-wave velocity structures of sediments and upper crust in the region off Ibaraki by applying ambient noise tomography to a dense array of short-period ocean bottom seismometers (OBSs). The cross-spectra were calculated using 27- or 142-day continuous seismic data, and the phase velocities of the fundamental and the first-higher Rayleigh wave modes are obtained in the frequency ranges of 0.1–0.25 Hz and 0.17–0.3 Hz, respectively. Our 1-D S-wave velocity inversion based on the trans-dimensional Markov chain Monte Carlo method revealed multiple sedimentary layers above the acoustic basement and the upper crustal structure. The 1-D structure was then used as a reference model to conduct ambient noise tomography and non-linear inversion of the 3-D S-wave velocity structure by collecting data of the local 1-D S-wave velocity structure. Our 3-D S-wave velocity structure revealed three main points: (1) The acoustic basement is situated at a depth of ~4 km depth; (2) the crustal structure is more complex than the that of the sedimentary layers; and (3) the southern region has a complex crustal structure in which subducting seamounts were identified by previous P-wave velocity tomographies.

1 Introduction

Ocean bottom seismometer (OBS) networks of both temporary and permanent deployment have been recently developed along subduction zones (e.g., Cascadia Initiative, S-net, DONET, HOBITSS). High-frequency waveform data from OBSs, most of which were obtained at frequencies higher than 0.1 Hz, can be used in receiver function analysis for evaluating shallow subduction structures (e.g., Reeves et al., 2015; Akuhara and Mochizuki, 2015) or waveform modeling to determine seismic source properties (e.g., Nakano et al., 2015; Takemura et al., 2020). Such studies help us to better understand the lithology, deformation, and earthquake processes of subduction zones. However, uncertainties in shallow thick sedimentary structures could bias the estimates of deeper structures and source locations owing to a trade-off between seismic velocity and depth. Intense reverberations within the sediment can also distort these estimates (e.g., Audet 2016). Thus, constraining the sedimentary structure is essential for addressing these limitations. Moreover, a well-constrained sediment structure, particularly the detailed topography of the acoustic basement, can enrich our understanding of the subduction process (e.g., Tsuji et al. 2015). Although active-source methods have been widely used for studying sedimentary structures (e.g., Tsuru et

al., 2002), conducting 3-D surveys is cost prohibitive. Although ambient noise tomography is an alternative tool that does not have the active-source requirement (Bussat and Kugler, 2011), its potential has not been fully explored.

This method has been widely used during the past decade to derive seismic structures (e.g., Shapiro et al., 2005). The basic principle of ambient noise seismic interferometry dates back to the pioneering work of Aki (Aki, 1957). Ambient noise tomographies reveal S-wave velocity structures using dispersion curves of surface-wave phase velocities (e.g., Lin et al., 2008; Ekström et al., 2009) or group velocities (e.g., Shapiro et al., 2005) calculated from cross-correlations of seismic noise data. Many studies have used onshore stations to show tomographic images of S-wave velocity structures of the crust and the uppermost mantle at the regional scale (e.g., Yang et al., 2008; Sun et al., 2010; Calkins et al., 2011; Bao et al., 2015) or the global scale (e.g., Nishida et al., 2009). More recently, dense seismic arrays have been used for imaging local-scale structures of the shallow crust (e.g., Wang et al., 2017).

For offshore regions, few ambient noise studies have used high-frequency data because the low S-wave velocity of thick sedimentary layer increases the wave number between stations, which creates strong attenuation. Most studies have analyzed data in periods ranging from several to dozens of seconds using data from broadband OBSs with station intervals of tens to hundreds of kilometers. Since Lin et al. (2006) suggested the possibility of ambient noise tomography across oceans, studies have resolved the seismic velocity structure of the crust and the uppermost mantle (e.g., Zha et al., 2014; Ball et al., 2016; Corela et al., 2017; Ryberg et al., 2017; Hable et al., 2019). For the regional scale, 1-D imaging of an oceanic lithosphere–asthenosphere system has been derived from ambient noise seismic interferometry applied to data from broadband OBSs (e.g., Harmon et al., 2007; Takeo et al., 2013; Lin et al., 2016).

Recently, Bussat and Kugler (2011) used a super-dense OBS array with a station interval of about 500 m. They used data in several frequencies to derive the structures of the sediments and the upper crust. Mordret et al. (2013, 2014) used an ocean-bottom cable array with a station interval of several meters in an oil industrial field. They also used data in several frequencies to resolve the shallow sedimentary structure to a depth of 700 m below sea level, within an area of ~10×10 km^2. Frequency–wavenumber analysis of ambient noise recorded by distributed acoustic sensing (DAS) is also feasible for revealing high-resolution 2-D shallow structures (e.g., Spica et al., 2020), although this method is not based on seismic interferometry. Despite the importance of 3-D high-resolution structures, few studies have resolved local-scale tomographic structures including sedimentary layers by using short-period OBSs with station intervals of less than 10 km.

In this study, we reveal 3-D S-wave velocity structures of sediments and the upper crust by applying ambient noise tomography to data from 30 short-period OBSs deployed off the Ibaraki region with station intervals of about 6 km. We measure the phase velocities of the fundamental and the first-higher modes of Rayleigh wave and derive the S-wave velocity structure. Although surface-wave inversion often suffers from a trade-off between the estimation of the layer thickness and that of S-wave velocity in the model obtained by surface-wave non-linear inversion, using both the fundamental and the first-higher modes provides a better constraint. The obtained S-wave velocity resolves multiple layers above the acoustic basement. Such high-resolution structures will make a significant contribution to waveform modeling of OBS data (e.g., waveform inversion and receiver-

function analysis), which will enable us to resolve better S-wave velocity structures in deeper parts or to determine accurate earthquake source mechanisms.

2 Study area and data

This study used data from a dense array with 30 OBSs deployed off the Ibaraki region in northeastern Japan along the Japan Trench subduction zone (Figure 1). This region lies at the southern end of the focal area of the 2011 off the Pacific coast of Tohoku earthquake (Tohoku-oki earthquake) and 300 km south of its epicenter. The largest aftershock (Mw 7.8) occurred 30 min after the mainshock in the landward side of the array. More than 10,000 aftershocks that occurred just beneath the network were observed (Nakatani et al., 2015). Recent studies have reported slow earthquake activities in the southern end of the region (e.g., Nishikawa et al., 2019).

Although high-resolution 3-D P-wave or S-wave velocity structures are not revealed, 2-D P-wave velocity structure have been imaged along with existing active-source seismic profiles (e.g., Mochizuki et al., 2008; Nakahigashi et al., 2012). A chain of seamounts exists on the incoming Pacific plate seaward of the trench (Figure 1, inset), whereas the seafloor topography appears to be fairly flat to the north. Mochizuki et al. (2008) suggested that a seamount has been subducting beneath the southern part of the region.

The OBS array is composed of 35 three-component short-period (1 Hz) seismometers (LE-3Dlite, Lennartz, Germany) with a station interval of approximately 6 km. First, 24 OBSs near the array center were deployed on October 18, 2020, and the surrounding 11 OBSs were added on February 15, 2011. Of these, 31 were successfully recovered by September 2011 (Nakatani et al., 2015). An active-source seismic survey was conducted during the observation, the results of which were used to determine the horizontal sensor orientation. The data from two OBSs were excluded. In the first case, the OBS missed seismic records from air-gun shots, and the amplitude level of the second OBS was found to be erroneously low, owing likely to a malfunction of its recorder.

During the observation period, the Mw 7.3 Sanriku-oki earthquake occurred on March 9, 2011, and was followed by the Mw 9.0 Tohoku-oki earthquake occurring on March 11, 2011. Many aftershocks followed these earthquakes. Ambient noise tomography requires an assumption of the isotropic and homogeneous source distribution in theory (e.g., Wapenaar, 2004). Because the intense aftershock activity breaks this assumption, we used data obtained before the Sanriku-oki earthquake. We analyzed only the vertical and radial components because the signal-to-noise ratio of the transverse component was worse than that of other components. Therefore, our dataset consisted of vertical and radial components of 20 OBSs for 142 days, vertical and radial components of nine OBSs for 22 days, and a vertical component of an OBS for 142 days.

3 Ambient noise interferometry: calculation of cross-spectra

In sections 3–6, the four steps of the analytic process are discussed, as illustrated in Figure 2: (1) calculation of the cross-spectra, (2) measurement of the phase velocities assuming a 1-D structure for inversion of the reference 1-D S-wave velocity structure, (3) measurement of the phase-velocity anomalies for inversion of the 2-D phase-velocity structure, and (4) inversion of the 3-D S-wave velocity structure by combining local 1-D S-wave velocity structures at every OBS station.

We applied a band-pass filter of 0.05–9.0 Hz to the data and decimated data from 200 to 20 Hz. We found that the ambient noise data obtained lower than about 0.1 Hz were useless owing to the low sensitivity of the short-period sensors. After deconvolving the data using the instrumental response function, we divided all data records into 10-min segments and removed linear trends. We discarded segments with contamination of transients (e.g., glitches or instrumental noise) from the dataset and applied one-bit normalization (e.g., Bensen et al., 2007) to suppress the effects of non-stationary phenomena such as earthquakes. One-bit normalization is a powerful and simple tool when used to observe ambient noise that still contains small earthquakes after removing many aftershocks and earthquake-like signals.

The observed power of ambient noise can also vary in the frequency domain. We calculated the Fourier spectra for all 10-min segments with spectrum whitening (e.g., Bensen et al., 2007) to suppress temporal changes in the frequency content of the microseisms. We then calculated the cross-spectra for each station pair p and each component γ as

$$\rho_{p,\gamma}^{\mathrm{obs}}(\omega) = \frac{f_{i,\gamma}(\omega) \cdot \bar{f}_{j,\gamma}(\omega)}{\left|f_{i,\gamma}(\omega)\right|\left|\bar{f}_{j,\gamma}(\omega)\right|}, \quad (1)$$

where $f_{i,\gamma}$ is the Fourier spectrum of one-bit normalized data for the i-th station, and the overline represents the complex conjugate. The value γ takes either the radial R component or the vertical Zcomponent. We applied this convention throughout the study.

Cross-correlation functions (CCFs), which are calculated by using the inverse Fourier transform of the cross-spectra, are dominated by Rayleigh wave (Figure 3). The fundamental mode of Rayleigh wave clearly appeared in the vertical component in the frequency range of 0.0625–0.3125 Hz (Figure 3a, c). The fundamental and the first-higher modes of Rayleigh wave appeared in the radial component (Figure 3b, d). For both modes, CCFs from 0.0625 Hz to 0.1875 Hz indicate higher phase velocities than those from 0.1875 Hz to 0.3125 Hz. In our calculations, a positive (negative) lag time of a CCF indicates Rayleigh waves from the northwest (southeast). Some CCFs showed larger Rayleigh-wave amplitudes in the negative lag times than those in the positive lag time, which means that more ambient noise traveled from the Pacific Ocean, where the dominant sources exist (e.g., Takagi et al., 2018).

4 1-D reference seismic velocity structure

In this section, we discuss two steps for performing inversion of the 1-D reference seismic velocity structure. First, we measured the dispersion curves of Rayleigh waves using the spatial auto-correlation (SPAC) method (Aki, 1957; Nishida et

al., 2008; Haney et al., 2012). Then, we performed inversion of the 1-D S-wave velocity structure using the trans-dimensional Markov chain Monte Carlo (MCMC) method (Bodin et al., 2012).

4.1 Measurement of dispersion curves of Rayleigh waves

Assuming a local 1-D seismic velocity structure beneath the entire area of the OBS array, we measured the phase velocities as a function of frequencies using the SPAC method (e.g., Nishida et al., 2008). We used only the real part of the observed cross-spectrum because the imaginary part reflects mainly the heterogeneity of the noise sources (e.g., Weaver et al., 2009).

For the vertical component ($\gamma = \mathrm{Z}$), the synthetic cross-spectrum at an angular frequency ω can be expressed as

$$\rho_{p,Z}^{\mathrm{syn}}(a, c^{1\mathrm{D}}; \omega) = a(\omega) J_0\left(\frac{\omega d_p}{c^{1\mathrm{D}}(\omega)}\right), \tag{2}$$

where a is the power spectrum, d_p is the station interval for p-th pair, $c^{1\mathrm{D}}$ is the assumed phase velocity, and J_0 is the zeroth-order Bessel function of the first kind. For the radial components ($\gamma = R$), if a wavelength considerably shorter than its station interval, we can neglect the contribution of Love waves (e.g., Takeo et al., 2013). With this assumption, the synthetic cross-spectrum can be written as

$$\rho_{p,R}^{\mathrm{syn}}(a, c^{1\mathrm{D}}; \omega) = a(\omega)\left[J_0\left(\frac{\omega d_p}{c^{1\mathrm{D}}(\omega)}\right) - J_1\left(\frac{\omega d_p}{c^{1\mathrm{D}}(\omega)}\right) \Big/ \left(\frac{\omega d_p}{c^{1\mathrm{D}}(\omega)}\right)\right], \tag{3}$$

where J_1 is the first-order Bessel function of the first kind.

We measured the phase velocity at a fixed angular frequency for the entire area by maximizing the variance reduction as

$$VR(a, c^{1D}; \omega) = 1 - \frac{\Delta_\gamma(a, c^{1\mathrm{D}}; \omega)}{\sum_p w_p \left[\rho_{p,\gamma}^{\mathrm{obs}}(\omega)\right]^2}, \tag{4}$$

where the squared difference $\Delta_\gamma(a, c^{1\mathrm{D}}; \omega)$ between the synthetic (equations (2) or (3)) and observed cross-spectra (equation (1)) is written as

$$\Delta_\gamma(a, c^{1\mathrm{D}}; \omega) = \sum_p w_p \left[\rho_{p,\gamma}^{\mathrm{obs}}(\omega) - \rho_{p,\gamma}^{\mathrm{syn}}(a, c^{1\mathrm{D}}; \omega)\right]^2. \tag{5}$$

Here, w_p is a weighting term set to the reciprocal of the square root of the station distance. We found that this choice offers sharp resolution for the phase velocity, whereas it caused side lobes with relatively large amplitudes.

Figure 4c–d shows the variance reduction (equation 5) against frequency and phase velocity. To obtain this diagram, we fixed a at a value stratifying $\frac{\partial \Delta}{\partial a} = 0$ at each angular frequency ω, which can be determined analytically. The fundamental mode of Rayleigh waves was clearly found in the vertical and the radial components, whereas the first-higher mode was identifiable only in the radial components. We note that the array geometry on regular grids (Figure 1) caused a checkerboard artifact in the variance reduction above 0.15 Hz, particularly in the radial component (Figure 4d). The sparse distribution of data along the distance (i.e., station separation) axis makes it difficult to constrain zero-crossings of the cross-spectrum (Figure 4a, b). Nevertheless, we can choose the appropriate mode branch in the following manner.

We first measured the phase velocity that maximizes the variance reduction at the highest frequency (0.25 Hz for the fundamental mode and 0.3 Hz for the first-higher mode). Then, for subsequent lower frequencies, we searched for the phase velocities that maximize the variance reduction in the vicinity of the phase velocity at the previous frequency. The resulting phase velocity range of the fundamental mode was 0.5–2.4 km/s at 0.1–0.25 Hz, and that of the first-higher mode was 0.8–1.5 km/s at 0.17–0.3 Hz, as represented by white dots in Figure 4c, d. Following Takeo et al. (2013), we estimated the uncertainties of the phase velocities using a bootstrap method (Efron, 1992). We randomly selected station pairs allowing for overlapping and made 100 sets of bootstrap samples. We measured the phase velocities using these bootstrap samples and estimated the measurement errors, which varied from 1.0×10^{-5} to 0.83.

We used the vertical component to measure the phase velocities of the fundamental mode of Rayleigh wave and the radial component to measure those of the first-higher mode because the vertical component for the fundamental mode showed higher variance reduction. The radial component is potentially contaminated by Love wave when a wavelength is comparable to or longer than the station interval (Aki, 1957); however, we obtained similar results for the fundamental mode at low frequencies when using the radial component. This consistency suggests that the effect of Love wave was not significant. This justified the use of the radial component for the higher mode, which also had shorter wavelengths than the station intervals, similar to those of the fundamental mode.

4.2 Inversion for 1-D S-wave velocity structure

We used the trans-dimensional MCMC method to perform inversion for the averaged 1-D S-wave velocity structure beneath the OBS array. We set a prior probability distribution of the parameters (number of layers, interface depth, and S-wave velocity of each layer) as a uniform distribution with sufficiently wide bounds to be regarded as non-informative (1–10 for the number of layers; 2.3–10 km for interface depths; and 0.1–5 km/s for S-wave velocities). Although the phase velocities of Rayleigh waves are sensitive to the seafloor depth, we fixed the value at 2.3 km, which is the average depth in this array. We included the effect of seafloor depth in the 3-D structure inversion analysis (section 6). We did not solve for P-wave velocities and densities; rather, we fixed them using the empirical scaling law by Brocher (2005). The S-wave velocity of the bottom layer was fixed at 4.6 km/s as the typical value of the S-wave velocity at the upper mantle because the bottom layer was sufficiently deep for our Rayleigh-wave inversion analysis.

The inversion began with a randomly generated velocity model. At each iteration, the model from previous iteration is slightly modified by either adding a layer, removing a layer, perturbing the S-wave velocity of a layer, or moving the bottom depth of a layer. Then, the synthetic dispersion curves were calculated using the method of Saito (1988) to evaluate the likelihood, which is defined in the form of multivariate Gaussian distribution with a diagonal covariance matrix for data error (e.g., Bodin et al. 2012). The standard deviations, or the diagonal elements, were set to a uniform value of 0.1 km/s, which was determined ad hoc. Finally, the model was judged to accept or not by the Metropolis–Hastings–Green criterion (Green, 1995). We repeated this iteration 500,000 times, but we did not save the models during the first 100,000 iterations. Afterward, we saved the models at every 100 iteration. We employed a parallel tempering algorithm to enhance the capability of global sampling, which

involved 20 non-tempered and 80 tempered MCMC chains (e.g., Sambridge, 2014). We obtain 10,000 models after the inversion, which were used to construct posterior probability distribution and related quantities such as marginal distribution. The obtained posterior probability distribution suggests that the region shallower than 4 km is well constrained despite the given loosely bounded uniform priors (Figure 5a–c). The median model showed a very low-velocity layer (LVL 1) immediately beneath the seafloor and another low-velocity layer (LVL 2) beneath the first. The thicknesses of LVL 1 and LVL 2 were 0.4 km and 1.4 km, and their S-wave velocities were 0.34 km/s and 0.85 km/s, respectively. Below these layers, the S-wave velocity sharply increased to 2.1 km/s at ~4 km in depth, which suggests the depth of the acoustic basement. This depth is consistent with 2-D reflection surveys (Tsuru et al., 2002; Nishizawa et al., 2009) and P-wave velocity tomography using data from active-source survey (Mochizuki et al., 2008).

We also obtained a low-velocity layer with an S-wave velocity of 2.1 km/s (LVL 3) just beneath the acoustic basement, although the marginal distribution indicated large uncertainty compared with LVLs 1 and 2. The thickness of LVL 3 was ~1.2 km. Beneath that layer, the S-wave velocity gradually increased to more than 3 km/s, which is consistent with the S-wave velocity of the upper crust.

5. 2-D Phase velocity map

We measured the phase velocity perturbation with respect to the reference 1-D phase velocity for each station pair. Following Nagaoka et al. (2012), we determined the phase velocity perturbation by fitting the synthetic cross-spectrum to the observed cross-spectrum $\rho_{p,\gamma}^{\mathrm{obs}}(\omega)$ for each path and for each frequency binned by 0.025 Hz with 0.0125 Hz overlap. The central angular frequency of the l-th bin for the fundamental mode ($\zeta = 0$) is given by

$$\omega_0^l = 2\pi(0.0125 \times l + 0.1) \quad (l = 1, 2, \dots, 12), \tag{6}$$

and that for the first-higher mode ($\zeta = 1$) is written as

$$\omega_1^l = 2\pi(0.0125 \times l + 0.175) \quad (l = 1, 2, \dots, 6). \tag{7}$$

From these equations, we used the central frequency for referring to each frequency bin.

First, we used the vertical component to measure the phase velocities of the fundamental mode of Rayleigh wave because the CCFs of the this component mostly have signals of the fundamental mode of Rayleigh wave only. The synthetic cross-spectrum of the fundamental mode including the phase velocity perturbation of each station pair $\rho'^{\mathrm{syn}}_{p,0}(b, e_0^l; \omega)$ is given by

$$\rho'^{\mathrm{syn}}_{p,0}(b, e_0^l; \omega) = a(\omega)b(\omega)J_0\left(\frac{\omega d_p}{(1 + e_0^l(\omega))c_0^{1\mathrm{D}}(\omega)}\right), \tag{8}$$

where b is the correction of the power spectrum, e_0^l is the assumed phase-velocity perturbation at the l-th frequency bin, and $c_0^{1\mathrm{D}}$ is the reference phase velocity of the fundamental mode of Rayleigh wave measured in section 4.1. We calculated the misfit function $\Delta'_{p,\zeta,l}\left(b, e_\zeta^l;\ \omega_\zeta^l\right)$ as

$$\Delta'_{p,\zeta,l}\left(b, e_\zeta^l; \omega_\zeta^l\right) = \int_{\omega_\zeta^l - 2\pi\cdot 0.0125}^{\omega_\zeta^l + 2\pi\cdot 0.0125} \left[\rho_{p,\gamma}^{\mathrm{obs}}(\omega) - \rho'^{\mathrm{syn}}_{p,\gamma}\left(b, e_\zeta^l; \omega\right)\right]^2 d\omega \tag{9}$$

for each frequency bin and each assumed phase velocity perturbation e_0. We minimized the misfit function $\Delta'_{p,\gamma}(b, e_0; \omega)$ analytically with respect to b. Hence, grid search was necessary only for e_ζ^l.

To avoid cycle skipping, we searched for the phase velocity perturbation only when b was positive, and we limited the search range of the phase velocity perturbations in two steps. In the first step, we calculated the misfit function, Δ', starting with 0.15 Hz ($l = 4$) because the signal-to-noise ratio was best. Since the possibility of the cycle skipping is related to the station distance, we changed the search range of the velocity perturbation in accordance with the station distance, as shown in Table 1. In the next step, we measured the phase velocity perturbations for the adjacent lower and higher frequency bins. This time, we further narrowed the search range referring to the results from the previous bin (Table 2). When no local minimum was found, we stopped measuring the phase velocity perturbations in the frequency range and the subsequent frequency ranges for the corresponding pair.

Next, we measured the phase velocity perturbation of the first-higher mode of Rayleigh wave using the radial component. Since this component contains both signals of the fundamental and the first-higher modes (Figure 3b, d), we fixed $a_0(\omega)$ and $a_1(\omega)$, which represent the power spectrum of the fundamental and the first-higher modes, respectively, at the values obtained during the analysis of section 3.1. The synthetic cross-spectrum is shown as

$$\rho'^{\mathrm{syn}}_{p,1}(b, e_1^l; \omega) = b(\omega)\left\{a_0(\omega)J_0\left(\frac{\omega d_p}{c_0^{2\mathrm{D}}(\omega)}\right) + a_1(\omega)\left[J_0\left(\frac{\omega d_p}{(1+e_1^l(\omega))c_1^{1\mathrm{D}}(\omega)}\right) - J_1\left(\frac{\omega d_p}{(1+e_1^l(\omega))c_1^{1\mathrm{D}}(\omega)}\right)\Big/\left(\frac{\omega d_p}{(1+e_1^l(\omega))c_1^{1\mathrm{D}}(\omega)}\right)\right]\right\},$$

where e_1^l is the assumed phase velocity perturbation at the l-th frequency bin, $c_0^{2\mathrm{D}}$ is the phase velocity of the fundamental mode of Rayleigh wave measured above, and $c_1^{1\mathrm{D}}$ is the reference phase velocity of the first-higher mode of Rayleigh wave. Again, b was analytically determined. We used a similar procedure for the first-higher mode to search for the phase velocity perturbation; the only difference was that in the first step, we used $l = 1$ in the search range shown in Table 1.

For the fundamental mode of Rayleigh wave, the resultant ranges of phase velocity perturbation was -10% to +10% at 0.1125 Hz and -30% to +30% at 0.20–0.25 Hz (Figure 6a–c). For the first-higher mode, the results showed -20% to +20% variations in the phase-velocity perturbations at 0.1875–0.20 Hz and -30% to +30% at 0.2125–0.25 Hz (Figure 7a–c).

To map the phase velocities in each frequency range, we conducted iterative non-linear inversion using the fast marching method (Rawlinson et al., 2005; Saygin, 2007), which solves the eikonal equation directly. We used a grid size of $0.032° \times 0.026°$ (approximately 3 km × 3 km). We then minimized the objective function $S(\boldsymbol{m})$ for each frequency and for each mode of Rayleigh wave as

$$S(\boldsymbol{m}^{2\mathrm{D}}) = (\boldsymbol{g}(\boldsymbol{m}^{2\mathrm{D}}) - \boldsymbol{\phi})^T \boldsymbol{C}_d^{-1}(\boldsymbol{g}(\boldsymbol{m}^{2\mathrm{D}}) - \boldsymbol{\phi}) + \epsilon(\boldsymbol{m}^{2\mathrm{D}} - \boldsymbol{m}_0)^T \boldsymbol{C}_m^{-1}(\boldsymbol{m}^{2\mathrm{D}} - \boldsymbol{m}_0). \tag{11}$$

Here, $\boldsymbol{g}(\boldsymbol{m}^{2\mathrm{D}})$ is the predicted travel time for the model $\boldsymbol{m}^{2\mathrm{D}}$, and $\boldsymbol{\phi}$ is the observed travel time data calculated as

$$\phi_{p,\zeta}^l = \frac{d_p}{\left(1+e_\zeta^l\right)c_\zeta^{1\mathrm{D}}(\omega_\zeta^l)}, \tag{12}$$

for the p-th pair and ζ-th mode of Rayleigh wave, where $\boldsymbol{C}_d$ is the data covariance matrix, $\boldsymbol{C}_m$ is the model covariance matrix, $\boldsymbol{m}_0$ is the initial model, $\boldsymbol{m}^{2\mathrm{D}}$ is the predicted model, and ϵ is the damping parameter. Following Rawlinson et al. (2006), we fixed the damping parameters to be 200 for the frequency bins of 0.1125–0.1375 Hz, 500 for 0.15–0.1625 Hz, and 1,000 for 0.175–0.25 Hz for the fundamental mode (Figure S2a, b). For the first-higher mode, the damping factor was set to 200 irrespective of the frequency (Figure S2c). We did not apply the smoothing parameter owing to the array geometry on the regular grids. We used the reference phase velocities as initial models, and we iterated 10 times to obtain the final model.

We calculated the root-mean-square (RMS) data residual as

$$\mathrm{RMS} = \sqrt{\frac{|\boldsymbol{\phi} - \boldsymbol{g}(\boldsymbol{m}^{2\mathrm{D}})|^2}{N}}, \tag{13}$$

where N is the number of observed travel time data. The RMS was improved from 39.00 s for the initial 1-D model to 10.32 s for the final 2-D model. For the fundamental mode, a low-velocity anomaly was located at the northern side of the array at lower frequencies (Figure 6e, f), and two low-velocity anomalies were located at the northern side and central part at higher frequencies (Figure 6g, h). For the first-higher mode, a low-velocity anomaly was also located at the northern side at lower frequencies (Figure 7d), and a low-velocity was found in the central part at higher frequencies (Figure 7e, f). The western part had higher velocity at lower frequencies for both modes (Figure 6e, 7d).

Following Zha et al. (2014), we estimated the uncertainties of the phase velocities using a bootstrap method (Efron, 1992). We randomly selected station pairs allowing for overlap and made 100 sets of bootstrap samples. We performed inversion of the phase velocity maps using these bootstrap samples and estimated the measurement errors (Figure S3). The standard deviations of the fundamental mode of Rayleigh wave are generally less than 0.05 km/s, and those of the first-higher mode were mainly less than 0.1 km/s. Therefore, the uncertainties were less than 10% for both the fundamental and first-higher modes. We conducted the checkerboard test and confirmed that velocity anomalies with a ~10 km horizontal length can be recovered (Figures S4 and S5).

6. 3-D S-wave velocity structure

We next obtained the phase velocity maps of 12 (6) frequency bands for the fundamental (first-higher) mode of Rayleigh wave. We applied 1-D non-linear inversion (Herrmann, 2013) for each horizontal grid q at a given location with longitude and latitude to construct a 3-D S-wave velocity structure. For each horizontal grid q, we minimized the misfit function Δ_q as

$$\Delta_q = \sum_{l,\zeta} \frac{\left[c_q^{\mathrm{obs}}(\omega_\zeta^l) - c_q^{\mathrm{syn}}(\omega_\zeta^l, \boldsymbol{m}_{\mathrm{q}}^{3\mathrm{D}})\right]^2}{C_q^{\mathrm{err}}(\omega_\zeta^l)^2}, \tag{14}$$

with respect to a given S-wave velocity model parameter $\boldsymbol{m}_{\mathrm{q}}^{3\mathrm{D}}$, where c_q^{obs} is the phase velocity for the q-th grid discussed in section 5, c_q^{syn} is the synthetic phase velocity for the model $\boldsymbol{m}_{\mathrm{q}}^{3\mathrm{D}}$, and c_q^{err} is the standard deviation of the phase velocities (Figure S3).

We created the initial model based on the median from the MCMC sampling (Figure 4). This initial model included three layers at the top with sharp velocity contrasts, corresponding to LVL 1–3; below these layers, the velocity gradually increased with depth. The latter deeper part is expressed as a stratification of thin layers with a constant thickness of 0.1 km. The unknown parameters to be determined by this inversion are the thickness and S-wave velocity of each layer. We iterated the inversion 30 times. The top three layers were changed in both thicknesses and S-wave velocity, although the bottom layers remained nearly the same when the thickness or S-wave velocity was changed.

We calculated the RMS data residual (RMS′) as

$$\mathrm{RMS}' = \sqrt{\frac{|\boldsymbol{c}^{\mathrm{obs}} - \boldsymbol{c}^{\mathrm{syn}}|^{\mathbf{2}}}{Q}}, \tag{15}$$

where Q is the number of horizontal grids. The RMS′ improved from 3.5×10^{-1} km/s in the initial 1-D model to 7.2×10^{-3} km/s in the final 3-D model.

The red, orange, and green regions in Figure 8, reflect LVL 1, LVL 2, and LVL 3, respectively. The thickness of LVL 1 varied from ~0.25 to ~0.55 km, which suggests that the variation is approximately 40%. The degree of thicknesses perturbation in LVL 2 (LVL 3) was generally less than 20% (10%). The variation in S-wave velocity in LVLs 2 and 3 was generally less than 10%. The area with the shallower acoustic basement exists at the northern to the central regions, where seafloor depth is shallow (Figure 9a).

The S-wave velocity of the blue region in Figure 8 is consistent with that of the crust. The topography of the boundary between the green and blue regions was more complex than that between the other layers (Figure 9b). Notably, this complexity was more evident in the southern region. To test the robustness of this feature, we repeated the same inversion analysis using different initial models with varying depths for the crust top. All of the experiment results indicated similar complexities in the northern region, which suggests this feature does not depend on initial models (Figure S6). The RMS′ was improved to 9.6×10^{-3} km/s from the initial model 2 and to 1.6×10^{-2} km/s from the initial model 3.

7 Comparison with previous P-wave velocity structures

As shown by the orange and green regions in Figure 8, our S-wave velocity increased sharply from LVL 2 to LVL 3 in both the 1-D and 3-D structures at a depth of about 4 km, which is considered to be the acoustic basement. Tsuru et al. (2002) and Nakahigashi et al. (2012) conducted seismic reflection and refraction surveys, respectively, the survey lines of which crossed our OBS array. Tsuru et al. (2002) identified a strong reflector at 4–5 km in depth, which has been interpreted as an erosional unconformity. The P-wave velocity of the model by Nakahigashi et al. (2012) sharply increased from ~2 km/s to ~4 km/s at a depth of ~5 km. Both features roughly agree with our results, which identify the acoustic basement at a depth of 4 km. In accordance with the geological interpretation of Takahashi et al. (2004), we interpret LVL 1 and LVL 2 (red to green region in Figure 8) to be sedimentary layers and LVL 3 (green region in Figure 8) to be Cretaceous sediment. The region in which the S-wave velocity is larger than 2.5 km/s (blue region in Figure 8) is considered to be continental crust.

Considering the results of Tsuru et al. (2002), the Vp/Vs ratio of LVL 1 is estimated to be 4.4 (P-wave velocity: 1.5 km/s, S-wave velocity: 0.34 km/s), and that of LVL 2 is 3.2 (P-wave velocity: 2.7 km/s, S-wave velocity: 0.84 km/s). The Vp/Vs ratio of LVL 3, at the top of the acoustic basement, is estimated to be 2.1 (P-wave velocity: 4.4 km/s, S-wave velocity: 2.1 km/s). These Vp/Vs ratios are consistent with the values of sediments. Although the P-wave and S-wave velocities were identified on the basis of different studies, the Vp/Vs ratios are roughly consistent with the scaling law of Brocher (2005).

The upper crust showed more structure complexity than the sedimentary layers, which is consistent with 2-D P-wave velocity structures (Tsuru et al., 2002; Mochizuki et al., 2008). The crustal structure in the southern region is more complex than that in the northern region (Figure 9). The P-wave velocity structure model of Mochizuki et al. (2008) suggests that several seamounts have been subducting in the southern part of the array. Other studies have indicated that subducting seamounts cause complexity in the crustal structure (e.g., Sun et al., 2020). Although the plate interface occurs at about 15 km in depth, the subducting seamounts created numerous faults that affected the top of the overriding crust above the plate interface. Thus, the complex crustal structure in the southern region can likely be attributed to seamount subduction.

8 Potential of OBS array for investigating 3-D sedimentary structure

In this study, we revealed the high-resolution S-wave velocity structure of the sediments and the upper crust using ambient noise tomography. Conventionally, P–S converted waves at the sediment–crust boundary generated by active sources (e.g., Yamamoto et al., 2017) or passive sources (e.g., Agius et al. 2018) have been used to determine the S-wave velocity and the thickness of the sedimentary layers. Studies using active sources provide high-resolution structure but limit the resolvable region owing to their high cost. Therefore, the resolvable area is usually 2-D. On the contrary, studies using both P–S converted wave by passive sources and ambient noise can be conducted at lower cost and are feasible for revealing 3-D structures. However, they are often limited by the trade-off between the estimates of S-wave velocity and thickness. The results of the present study can be used to better constrain both parameters and to reveal the high-resolution S-wave velocity structure for the following reasons.

We used the fundamental mode in addition to the first-higher mode in this study. We demonstrate the usefulness of the first-higher mode by conducting the trans-dimensional MCMC inversion using only the fundamental mode. We again emphasize that this method imposes almost no prior constraints because we set a prior probability as a uniform distribution. As a result, we can confirm that the two top layers, LVL 1 and LVL 2, cannot be resolved if only the fundamental mode is used (Figure 10). Because the first-higher mode is more sensitive to the shallowest part (Figure S1), the joint use of the two modes was considered to give respective constrains on these LVLs. In addition, the joint use of the multiple modes increased the resolution of the deeper region. When using only the fundamental mode, we obtained the maximum marginal probability at 4.6 km/s beneath the acoustic basement (Figure 10). We associate this anomalously high velocity with an artifact owing to the fixed velocity for the bottom layer, which means no constraint was added to the depths. The first-higher mode is more sensitive to crustal structures (Figure S1), which helped to resolve the crust. For further improvement of the velocity estimation, the

technique of Nakamura (Nakamura 1989; Lin et al., 2014; Berg et al., 2018) and the joint inversion of ambient noise and receiver functions (e.g., Bodin et al., 2012; Ball et al., 2014) could be feasible. However, such research is beyond the scope of this study.

In addition, we were able to use high-frequency data (~0.25 Hz of the fundamental mode and ~0.3 Hz for the first-higher mode), aided by the dense OBS array with station intervals of about 6 km. In general, ambient noise tomography studies using offshore stations analyze the data of periods ranging from several to dozens of seconds because their station intervals are tens to hundreds of kilometers (e.g., Hable et al., 2019). Thus, the S-wave velocity structures were revealed mainly beneath the crust only. Shallow sedimentary structure would not be recovered by such sparse networks owing to the lower signal-to-noise ratio of the high-frequency data. Super dense arrays with station intervals of about 500 m have been deployed in oil industrial fields (Bussat and Kugler, 2011; Mordret et al., 2013; 2014); however, the development of such an array for a broader region remains challenging. The present study demonstrates that short-period OBS arrays with station intervals of 6 km deployed portably for less than one month are capable of resolving fine-scale sedimentary structure above the acoustic basement at ~0.1–1.0 km vertically and ~10 km horizontally.

Such a high-resolution S-wave velocity structure of seafloor sediments will enhance seismic waveform modeling of body waves at high frequencies, at generally greater than 0.1 Hz, for studying the deeper structures (e.g., Harmon et al., 2007) or seismic source properties beneath the ocean (e.g., Nakano et al., 2015; Takemura et al., 2020). This is because the velocity contrast across the acoustic basement strongly affects the waveform amplitude. Studies using short-period OBSs generally use only extracted information of the phase arrivals such as travel time and amplitude polarity. However, our results prove the potential to use OBS waveform records directly for studies on velocity structures and earthquake source mechanisms with higher spatio–temporal resolution.

9 Conclusion

We derived the S-wave velocity structures of sediments and the upper crust by applying ambient seismic noise tomography using continuous seismic data of 22 or 142 days from the dense array of short-period OBSs deployed off the Ibaraki region. Our S-wave velocity model included three low-velocity layers at the top, with S-wave velocities of 0.34, 0.85, and 2.1 km/s, respectively. The top two of the three layers are considered to be sediments, and the bottom layer is considered to be Cretaceous sediment. The depth of the acoustic basement is considered to be ~4 km from the seafloor, which is consistent with previous P-wave velocity tomography by active source surveys. In addition, our model shows a complex crust structure in the southern region, where subducting seamounts have been indicated by previous P-wave velocity tomography. Further, we determined that using both the fundamental and the first-higher modes increases the resolution, which is facilitated by the dense OBS array with station intervals of about 6 km. Our model will make a significant contribution to waveform modeling of OBS data.

Acknowledgments

This study is supported by JSPS KAKENHI Grant Numbers 19J20692. Trans-dimensional inversion is performed using a computer program package SEIS_FILO, available at http://doi.org/10.5281/zenodo.4150550. TA is funded by JSPS Grant number JP19K21892. Our cross-correlation functions are available at http://doi.org/10.5281/zenodo.4433466. We thank Shinji Yoneshima for providing us with the orientations of OBS horizontal components.

References

Agius, M. R., Harmon, N., Rychert, C. A., Tharimena, S., and Kendall, J. M. M.: Sediment characterization at the equatorial Mid-Atlantic Ridge from P-to-S teleseismic phase conversions recorded on the PI-LAB experiment, Geophys. Res. Lett., 45, 12–244, doi: 10.1029/2018GL080565, 2018.

Aki, K.: Space and time Spectra of stationary stochastic waves, with special reference to microseisms, Bull. Earthquake Res. Inst. Univ. Tokyo, 35, 415–456, 1957.

Akuhara, T., and Mochizuki, K.: Hydrous state of the subducting Philippine Sea plate inferred from receiver function image using onshore and offshore data, J. Geophys. Res., 120, 8461–8477, 2015.

Audet, P.: Receiver functions using OBS data: Promises and limitations from numerical modelling and examples from the Cascadia Initiative, Geophys. J. Int., 205, 1740–1755, 2016.

Ball, J. S., Sheehan, A. F., Stachnik, J. C., Lin, F. C., Collins, J. A.: A Joint Monte Carlo Analysis of Seafloor Compliance, Rayleigh Wave Dispersion and Receiver Functions at Ocean Bottom Seismic Stations offshore New Zealand, Geochem., Geophys., Geosys., 15, 5051–5068, doi:10.1002/2014GC005412, 2014.

Ball, J. S., Sheehan, A. F., Stachnik, J. C., Lin, F. C., Yeck, W. L., and Collins, J. A.: Lithospheric shear velocity structure of South Island, New Zealand, from amphibious Rayleigh wave tomography, J. Geophys. Res., 121, 3686–3702, 2016.

Bao, X., Song, X., and Li, J.: High-resolution lithospheric structure beneath Mainland China from ambient noise and earthquake surface-wave tomography, Earth Planet. Sci. Lett., 417, 132–141, 2015.

Bensen, G. D., Ritzwoller, M. H., Barmin, M. P., Levshin, A. L., Lin, F., Moschetti, M. P., Shapiro, N. M., and Yang, Y.: Processing seismic ambient noise data to obtain reliable broad-band surface wave dispersion measurements, Geophys. J. Int., 169, 1239–1260, 2007.

Berg, E. M., Lin, F. C., Allam, A., Qiu, H., Shen, W., Ben-Zion, Y.: Tomography of southern California via Bayesian joint inversion of Rayleigh wave ellipticity and phase velocity from ambient noise cross-correlations, J. Geophys. Res., 123, 9933–9949, 2018.

Bodin, T., Sambridge, M., Tkalčić, H., Arroucau, P., Gallagher, K., and Rawlinson, N.: Transdimensional inversion of receiver functions and surface wave dispersion, J. Geophys. Res., 117, B02301, doi: 10.1029/2011JB008560, 2012.

Brocher, T. M.: Empirical relations between elastic wavespeeds and density in the Earth's crust, B. Seismol. Soc. Am., 95, 2081–2092, 2005.

Bussat, S., and Kugler, S.: Offshore ambient-noise surface-wave tomography above 0.1 Hz and its applications, The Leading Edge, 30, 514–524, 2011.

Calkins, J. A., Abers, G. A., Ekström, G., Creager, K. C., and Rondenay, S.: Shallow structure of the Cascadia subduction zone beneath western Washington from spectral ambient noise correlation, J. Geophys. Res., 116, B07302, doi: 10.1029/2010JB007657, 2011.

Corela, C., Silveira, G., Matias, L., Schimmel, M., and Geissler, W. H.: Ambient seismic noise tomography of SW Iberia integrating seafloor-and land-based data, Tectonophysics, 700, 131–149, 2017.

Ekström, G., Abers, G. A., and Webb, S. C.: Determination of surface-wave phase velocities across USArray from noise and Aki's spectral formulation, Geophys. Res. Lett., 36, L18301, doi: 10.1029/2009GL039131, 2009.

Hable, S., Sigloch, K., Stutzmann, E., Kiselev, S., and Barruol, G.: Tomography of crust and lithosphere in the western Indian Ocean from noise cross-correlations of land and ocean bottom seismometers, Geophys. J. Int., 219, 924–944, 2019.

Haney, M. M., Mikesell, T. D., van Wijk, K., and Nakahara, H.: Extension of the spatial autocorrelation (SPAC) method to mixed-component correlations of surface waves, Geophys. J. Int, 191, 189–206, 2012.

Harmon, N., Forsyth, D. W., Lamm, R., and Webb, S. C.: P and S wave delays beneath intraplate volcanic ridges and gravity lineations near the East Pacific Rise, J. Geophys. Res., 112, doi: 10.1029/2006JB004392, 2007.

Lin, F. C., Ritzwoller, M. H., Shapiro, N. M.: Is ambient noise tomography across ocean basins possible?, Geophys. Res. Lett., 33, L14304, doi:10.1029/2006GL026610, 2006.

Lin, F. C., Moschetti, M. P., Ritzwoller, M. H.: Surface wave tomography of the western United States from ambient seismic noise: Rayleigh and Love wave phase velocity maps, Geophys. J. Int., 173, 281–298, 2008.

Lin, F. C., Tsai, V. C., Schmandt, B.: 3-D crustal structure of the western United States: application of Rayleigh-wave ellipticity extracted from noise cross-correlations, Geophys. J. Int., 198, 656–670, 2014.

Lin, P. Y. P., Gaherty, J. B., Jin, G., Collins, J. A., Lizarralde, D., Evans, R. L., and Hirth, G.: High-resolution seismic constraints on flow dynamics in the oceanic asthenosphere, Nature, 535, 538–541, 2016.

Mochizuki, K., Yamada, T., Shinohara, M., Yamanaka, Y., and Kanazawa, T.: Weak interplate coupling by seamounts and repeating M~ 7 earthquakes, Science, 321, 1194–1197, 2008.

Mordret, A., Landès, M., Shapiro, N. M., Singh, S. C., Roux, P., and Barkved, O. I.: Near-surface study at the Valhall oil field from ambient noise surface wave tomography, Geophys. J. Int., 193, 1627–1643, 2013.

Mordret, A., Landès, M., Shapiro, N. M., Singh, S. C., and Roux, P.: Ambient noise surface wave tomography to determine the shallow shear velocity structure at Valhall: depth inversion with a Neighbourhood Algorithm, Geophys. J. Int., 198, 1514–1525, 2014.

Nagaoka, Y., Nishida, K., Aoki, Y., Takeo, M., and Ohminato, T.: Seismic imaging of magma chamber beneath an active volcano, Earth Planet. Sci. Lett., 333, 1–8, 2012.

Nakahigashi, K., Shinohara, M., Mochizuki, K., Yamada, T., Hino, R., Sato, T., Uehira, K., Ito, Y., Murai, Y., and Kanazawa, T.: P-wave velocity structure in the southernmost source region of the 2011 Tohoku earthquakes, off the Boso Peninsula, deduced by an ocean bottom seismographic survey, Earth Planets Space, 64, 1149–1156, 2012.

Nakamura, Y.: A method for dynamic characteristics estimation of subsurface using microtremor on the ground surface, Quaterly Report Railway Tech. Res. Inst., 30, 25–30., 1989.

Nakatani, Y., Mochizuki, K., Shinohara, M., Yamada, T., Hino, R., Ito, Y., Murai, Y., and Sato, T.: Changes in seismicity before and after the 2011 Tohoku earthquake around its southern limit revealed by dense ocean bottom seismic array data, Geophys. Res. Lett., 42, 1384–1389, 2015.

Nakano, M., Nakamura, T., & Kaneda, Y.: Hypocenters in the Nankai Trough Determined by Using Data from Both Ocean-Bottom and Land Seismic Networks and a 3D Velocity Structure Model: Implications for Seismotectonic Activity, B. Seismol. Soc. Am., 105, 1594-1605, 2015

Nishida, K., Kawakatsu, H., and Obara, K.: Three-dimensional crustal S wave velocity structure in Japan using microseismic data recorded by Hi-net tiltmeters, J. Geophys. Res., 113, B10302, doi:10.1029/2007JB005395, 2008.

Nishida, K., Montagner, J. P., and Kawakatsu, H.: Global surface wave tomography using seismic hum, Science, 326, 112–112, 2009.

Nishikawa, T., Matsuzawa, T., Ohta, K., Uchida, N., Nishimura, T., and Ide, S.: The slow earthquake spectrum in the Japan Trench illuminated by the S-net seafloor observatories, Science, 365, 808–813, 2019.

Reeves, Z., Lekić, V., Schmerr, N., Kohler, M., and Weeraratne, D.: Lithospheric structure across the C alifornia C ontinental B orderland from receiver functions, Geochemistry, Geophysics, Geosystems, 16, 246–266, 2015.

Ryberg, T., Geissler, W. H., Jokat, W., and Pandey, S.: Uppermost mantle and crustal structure at Tristan da Cunha derived from ambient seismic noise, Earth Planet. Sci. Lett., 471, 117–124, 2017.

Sambridge, M.: A parallel tempering algorithm for probabilistic sampling and multimodal optimization, Geophys. J. Int., 196, 357–374, 2014.

Shapiro, N. M., Campillo, M., Stehly, L., and Ritzwoller, M. H.: High-resolution surface-wave tomography from ambient seismic noise, Science, 307, 1615–1618, 2005.

Spica, Z. J., Nishida, K., Akuhara, T., Pétrélis, F., Shinohara, M., and Yamada, T.: Marine Sediment Characterized by Ocean-Bottom Fiber-Optic Seismology, Geophys. Res. Lett., 47, e2020GL088360, doi: 10.1029/2020GL088360, 2020.

Sun, X., Song, X., Zheng, S., Yang, Y., and Ritzwoller, M. H.: Three dimensional shear wave velocity structure of the crust and upper mantle beneath China from ambient noise surface wave tomography, Earthquake Sci., 23, 449–463, 2010.

Sun, T., Saffer, D., and Ellis, S.: Mechanical and hydrological effects of seamount subduction on megathrust stress and slip, Nature Geoscience, 13, 249–255, 2020.

Takagi, R., Nishida, K., Maeda, T., and Obara, K.: Ambient seismic noise wavefield in Japan characterized by polarization analysis of Hi-net records, Geophys. J. Int., 215, 1682–1699, 2018.

Takahashi, N., Kodaira, S., Tsuru, T., Park, J. O., Kaneda, Y., Suyehiro, K., Kinoshita, H., Abe, S., Nishino, M., and Hino, R.: Seismic structure and seismogenesis off Sanriku region, northeastern Japan, Geophys. J. Int., 159, 129–145, 2004.

Takemura, S., Yabe, S., and Emoto, K.: Modelling high-frequency seismograms at ocean bottom seismometers: effects of heterogeneous structures on source parameter estimation for small offshore earthquakes and shallow low-frequency tremors, Geophys. J. Int., 223, 1708–1723, 2020.

Takeo, A., Nishida, K., Isse, T., Kawakatsu, H., Shiobara, H., Sugioka, H., and Kanazawa, T.: Radially anisotropic structure beneath the Shikoku Basin from broadband surface wave analysis of ocean bottom seismometer records, J. Geophys. Res., 118, 2878–2892, 2013.

Tsuru, T., Park, J. O., Miura, S., Kodaira, S., Kido, Y., and Hayashi, T.: Along-arc structural variation of the plate boundary at the Japan Trench margin: Implication of interplate coupling, J. Geophys. Res., 107, 2357, doi:10.1029/2001JB001664, 2002.

Wang, Y., Lin, F. C., Schmandt, B., and Farrell, J.: Ambient noise tomography across Mount St. Helens using a dense seismic array, J. Geophys. Res., 122, 4492–4508, 2017.

Wapenaar, K.: Retrieving the elastodynamic Green's function of an arbitrary inhomogeneous medium by cross correlation, Phys. Rev. Lett., 93, 254301, doi:10.1103/PhysRevLett.93.254301, 2004.

Weaver, R., Froment, B., and Campillo, M.: On the correlation of non-isotropically distributed ballistic scalar diffuse waves, J. Acoust. Soc. Am., 126, 1817–1826, 2009.

Yamamoto, Y., Takahashi, T., Kaiho, Y., Obana, K., Nakanishi, A., Kodaira, S., & Kaneda, Y.: Seismic structure off the Kii Peninsula, Japan, deduced from passive-and active-source seismographic data, Earth Planet. Sci. Lett., 461, 163–175, 2017.

Yang, Y., Ritzwoller, M. H., Lin, F. C., Moschetti, M. P., Shapiro, N. M.: Structure of the crust and uppermost mantle beneath the western United States revealed by ambient noise and earthquake tomography, J. Geophys. Res., 113, B12310, doi:10.1029/2008JB005833, 2008.

Zha, Y., Webb, S. C., Wei, S. S., Wiens, D. A., Blackman, D. K., Menke, W., Dunn, R. A., and Conder, J. A.: Seismological imaging of ridge–arc interaction beneath the Eastern Lau Spreading Center from OBS ambient noise tomography, Earth Planet. Sci. Lett., 408, 194–206, 2014.

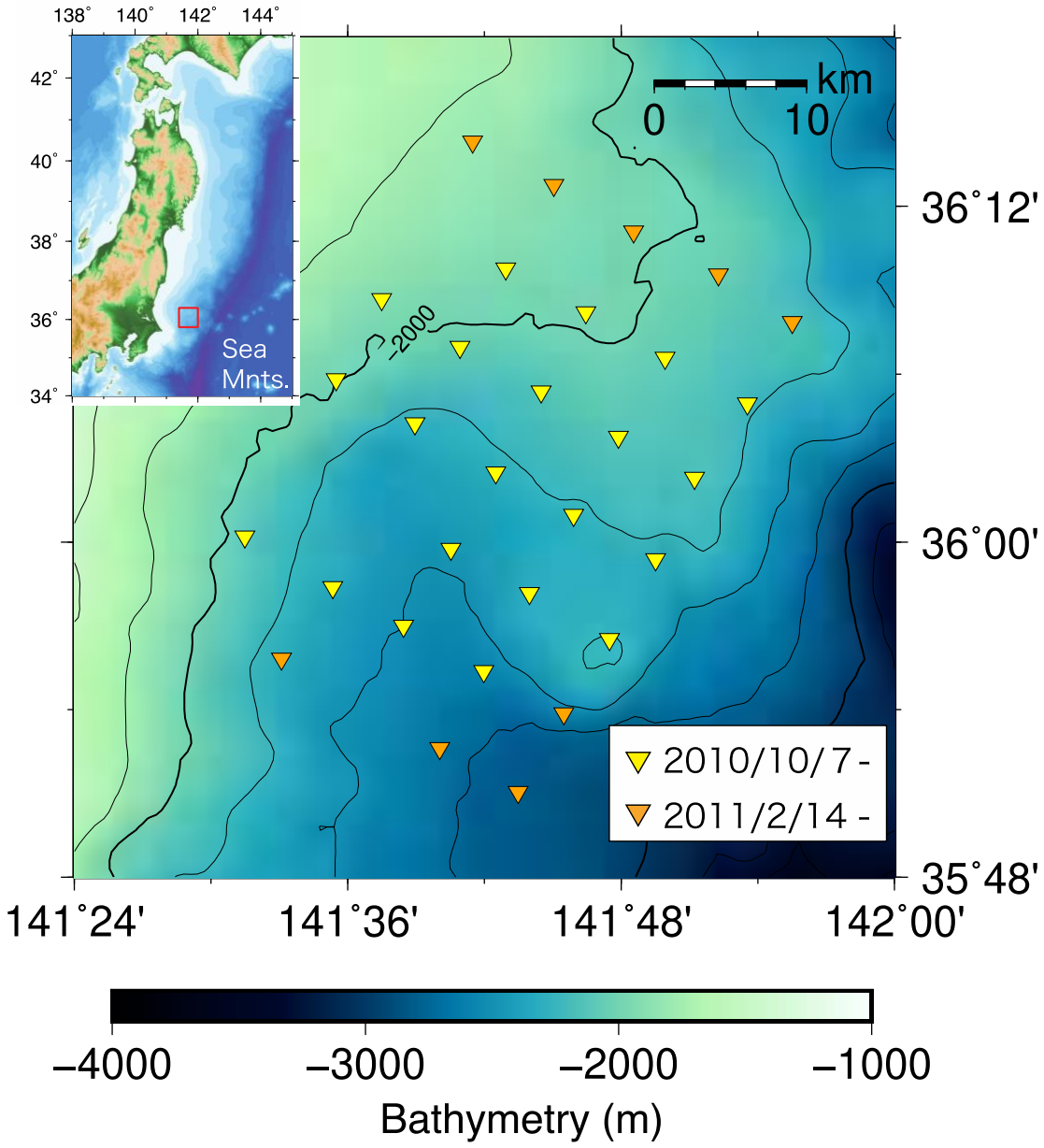

Figure 1. Stations of the OBS array in the region off Ibaraki. The station intervals are about 6 km. Yellow triangles show stations deployed on October 18, 2010, and orange triangles show those deployed on February15, 201**1.**

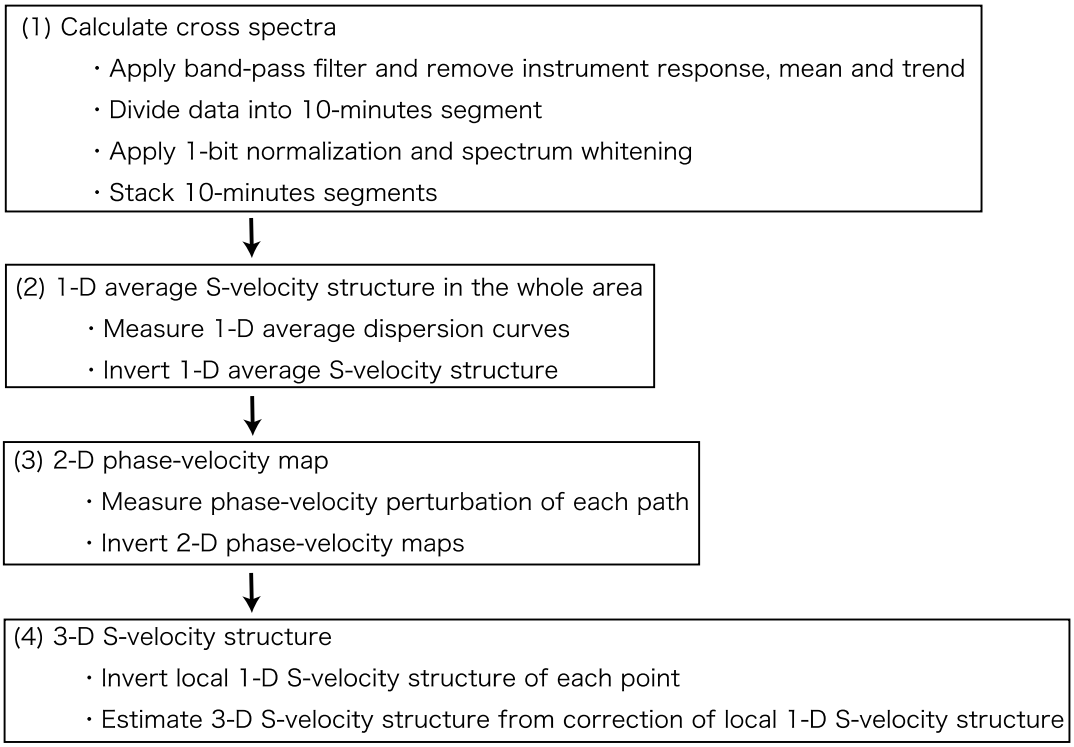

505 **Figure 2.** Schematic diagram of the analysys flow. In step (1), we calculated the cross-spectrum of each station pair. In step (2), we inferred the 1-D average S-wave velocity structure. In step (3), we inferred the 2-D phase-velocity structure. In step (4), we finally inferred the 3-D S-wave velocity structure.

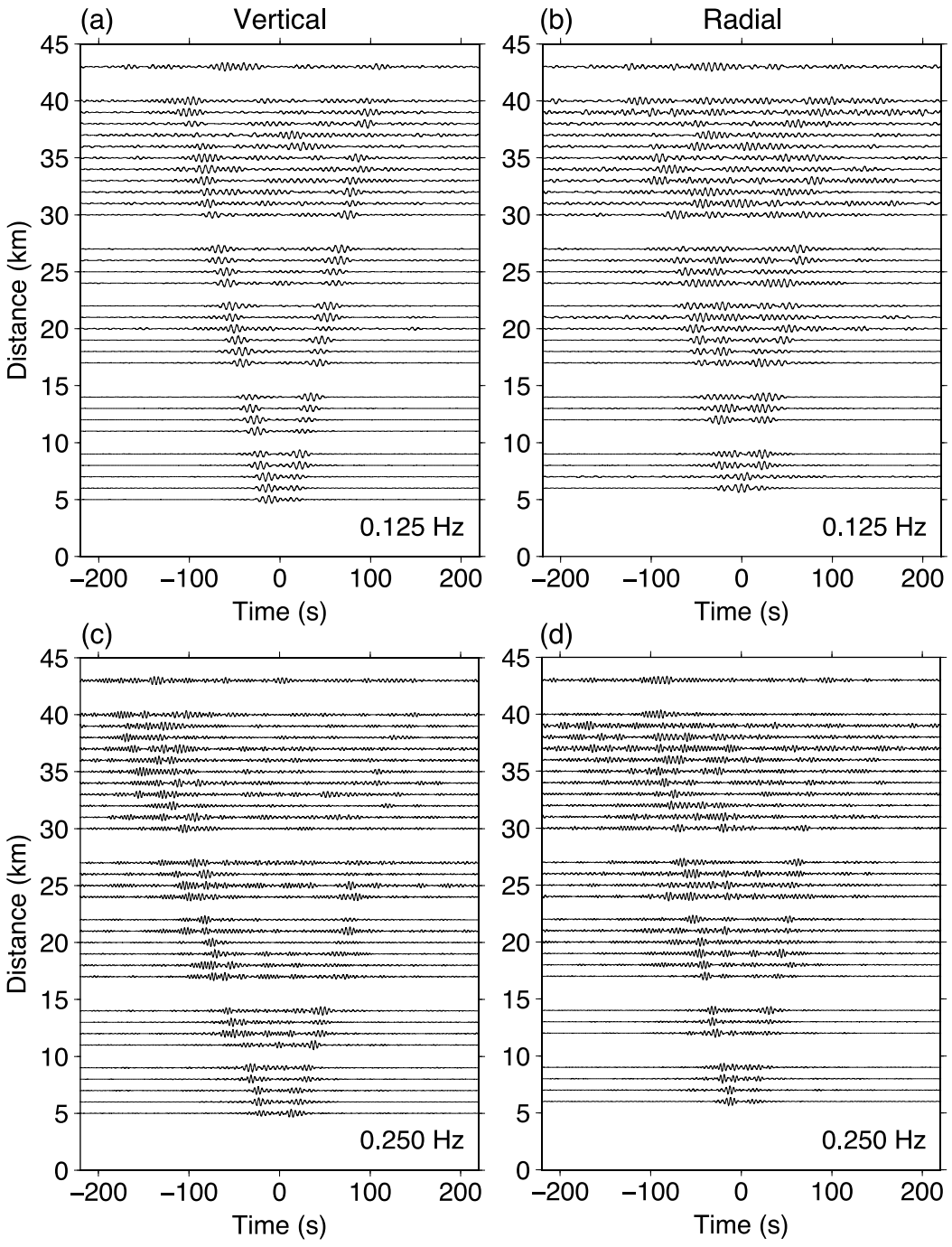

Figure 3. Stacked cross-correlation functions sorted in 1 km bins of interstation distance for all station pairs. The amplitudes are normalized by their maximum value. (a – b) Cross-correlation functions of the 0.0625–0.1875 Hz frequency range; (c – d) those of the 0.1875–0.3125 Hz frequency range. (a, c) Cross-correlation functions of the vertical components; (b, d) those of the radial components.

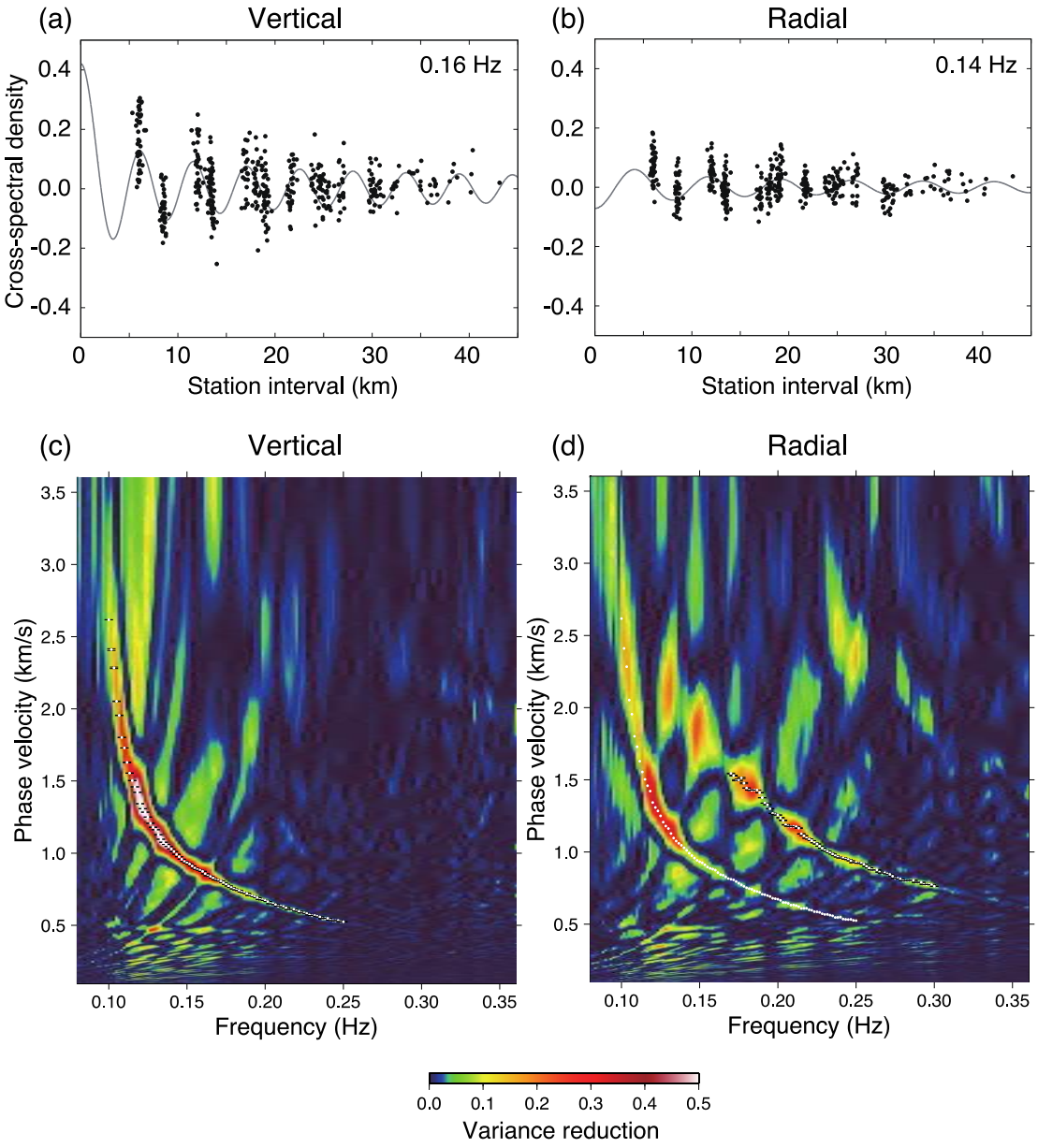

Figure 4. (a)-(b) Examples of fitting between the observed cross-spectra (solid black circles) and the synthetic curves obtained by equations (2) and (3) (gray lines). (a) Vertical component at 0.16 Hz. The assumed phase velocity is 0.87 km/s. (b) Radial component at 0.14 Hz. The assumed phase velocity is 1.05 km/s. (c – d) Variance reduction ($VR = 1 - \Delta$) between the observed cross-spectra and the synthetic curve for each component. The fundamental mode of Rayleigh wave was found in both the vertical and radial components. The first-higher mode of Rayleigh wave was clear only in the radial component. The white points show the measured 1-D average phase velocities of the fundamental and first-higher mode of Rayleigh wave.

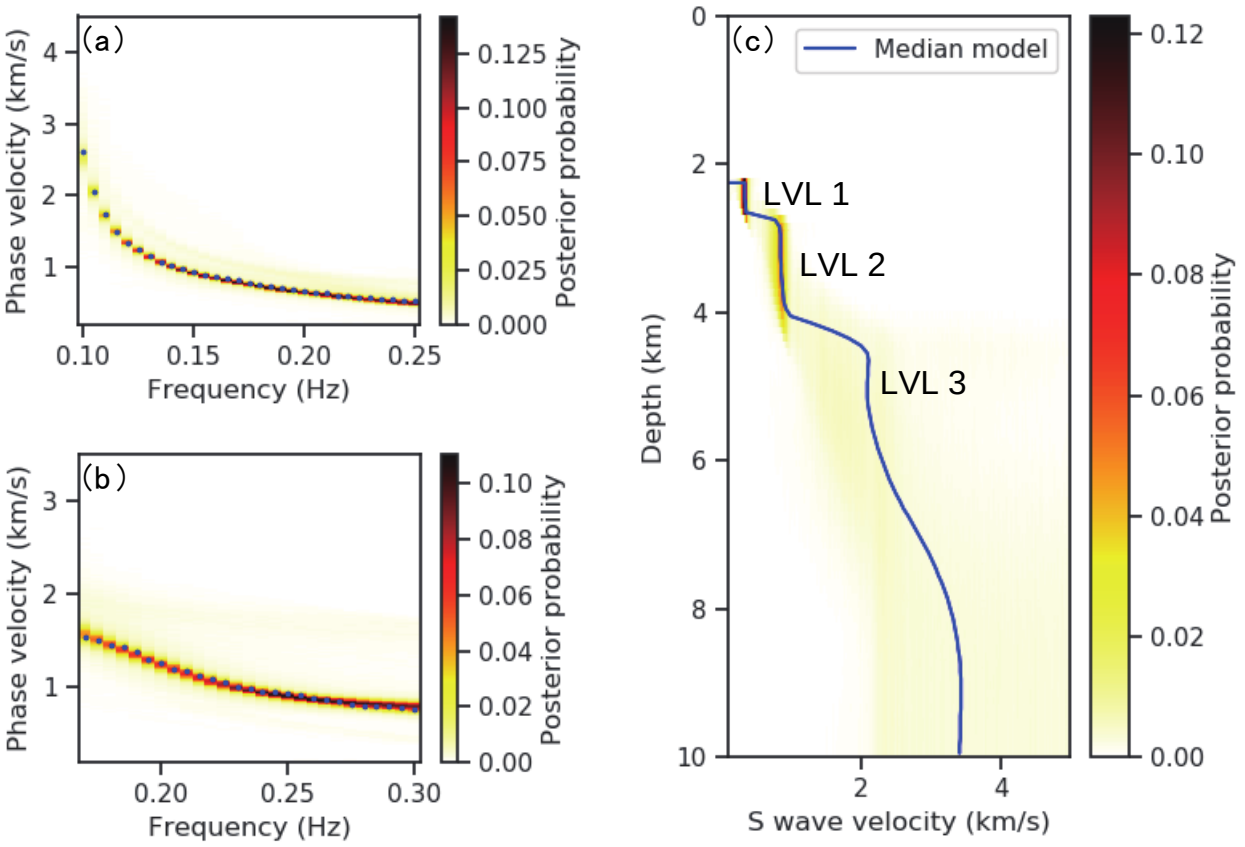

Figure 5. 1-D S-wave velocity structure inversion using both the fundamental and the first-higher modes of Rayleigh wave. (a) Phase velocity of the fundamental mode of Rayleigh wave. Blue points show the average phase velocities. The posterior probabilities were calculated for 1-D average S-wave velocity structures using the MCMC method. (b) Phase velocity of the first-higher mode of Rayleigh wave. Blue points show the 1-D average phase velocities. (c) S-wave velocity structure inferred by the MCMC method. The blue line shows the median velocity at each 0.1 km depth grid point. The bottom two figures show 1-D S-wave velocity structure inversion using only the fundamental mode of Rayleigh wave.

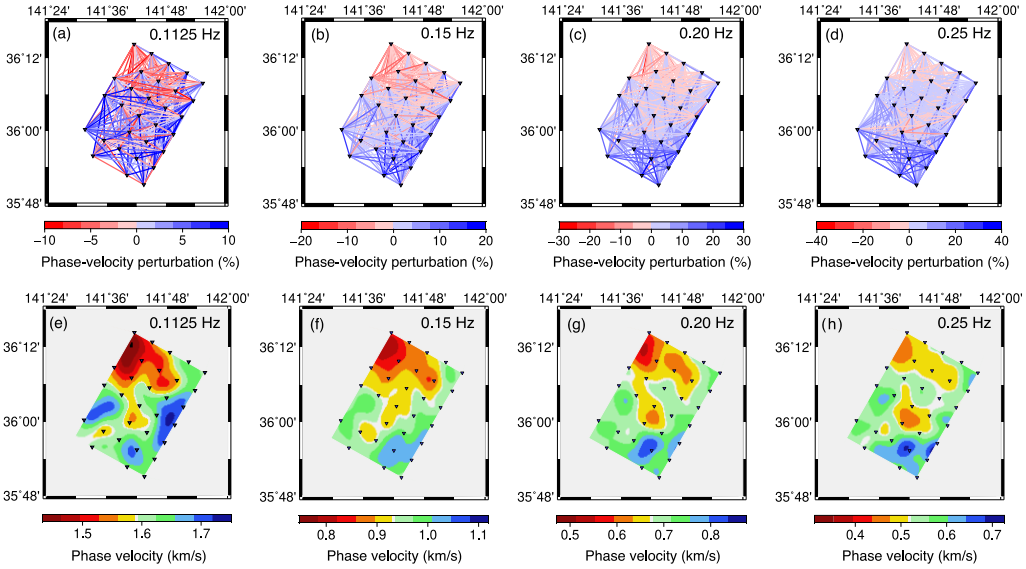

Figure 6. 2-D phase velocity inversion of the fundamental mode of Rayleigh wave. (a – d) Phase velocity perturbation of each station pair with respect to the 1-D average phase velocity in the entire area; (e – h) phase-velocity maps of the fundamental-mode of Rayleigh wave. (a, e) The case for the 0.1 - 0.125 Hz frequency range; (b, f) that for the 0.1375 - 0.1625 Hz frequency range; (c, g) that for the 0.1875 - 0.2125 Hz frequency range; (d, h) that for the 0.2375 - 0.2625 Hz frequency range. Blue triangles show the station locations.

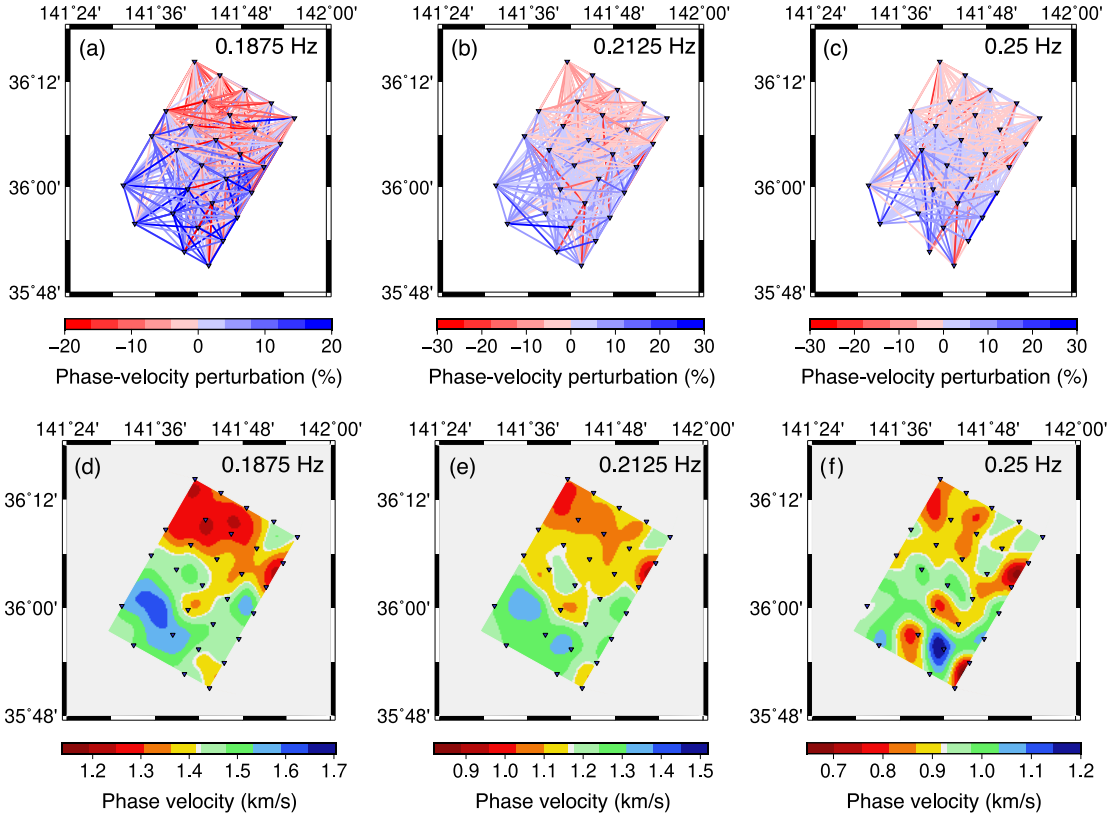

Figure 7. 2-D phase velocity inversion of the first-higher mode of Rayleigh wave. The notations are the same as those in Figure 6. (a, d) The case for the 0.175 - 0.20 Hz frequency range; (b, e) that for the 0.20 - 0.225 Hz frequency range; (c, f) that for the 0.2375 - 0.2625 Hz frequency range. Blue triangles show the station locations.

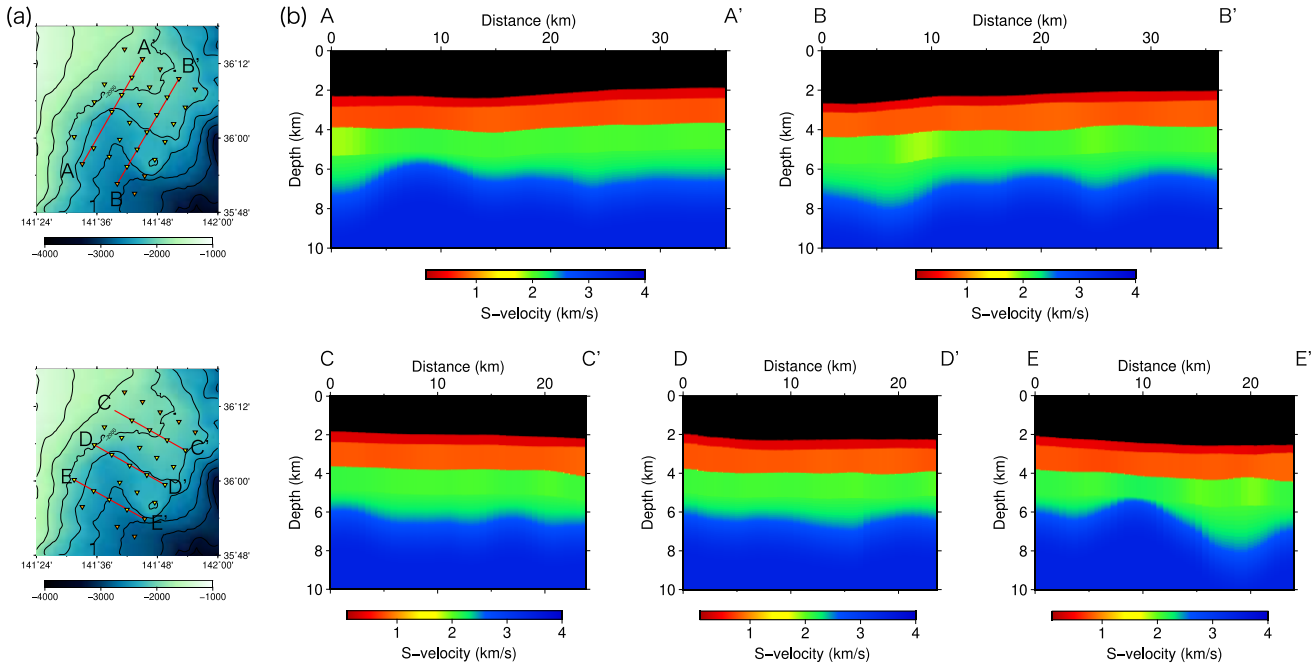

560 **Figure 8.** Cross-sections of 3-D S-wave velocity structure. (a) Locations of cross-sections. (b) S-wave velocities along the A–A′, B–B′, C–C′, D–D′, and E–E′ lines.

565

570

575

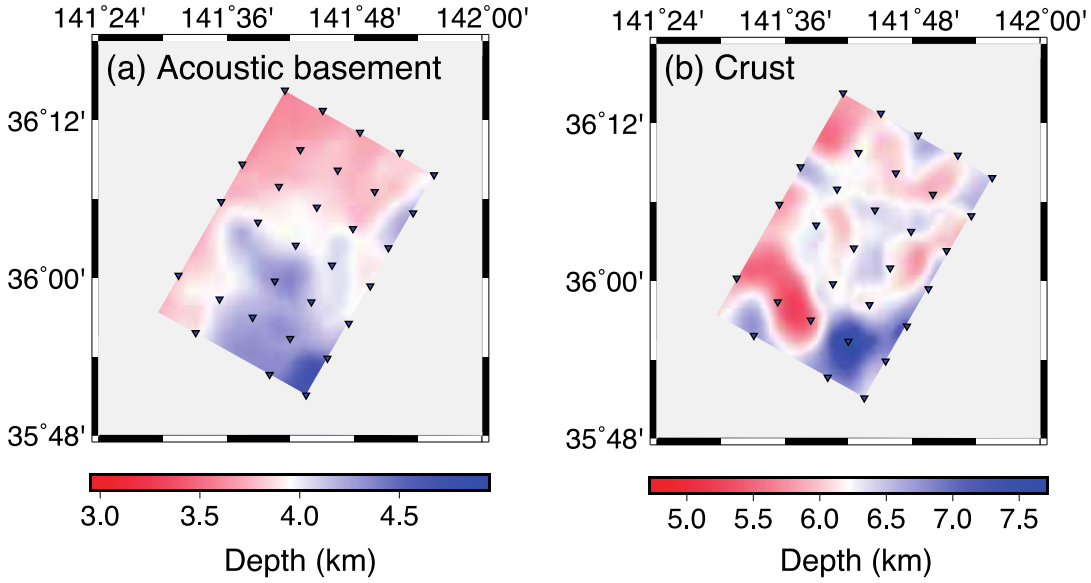

580 **Figure 9.** Depth variation of the (a) acoustic basement and (b) the top of the crust. The depth of the acoustic basement is assumed to be the bottom of LVL 2, and that of the top of the crust is assumed to be the depth at which the S-wave velocity increases to greater than 2.4 km/s.

585

590

595

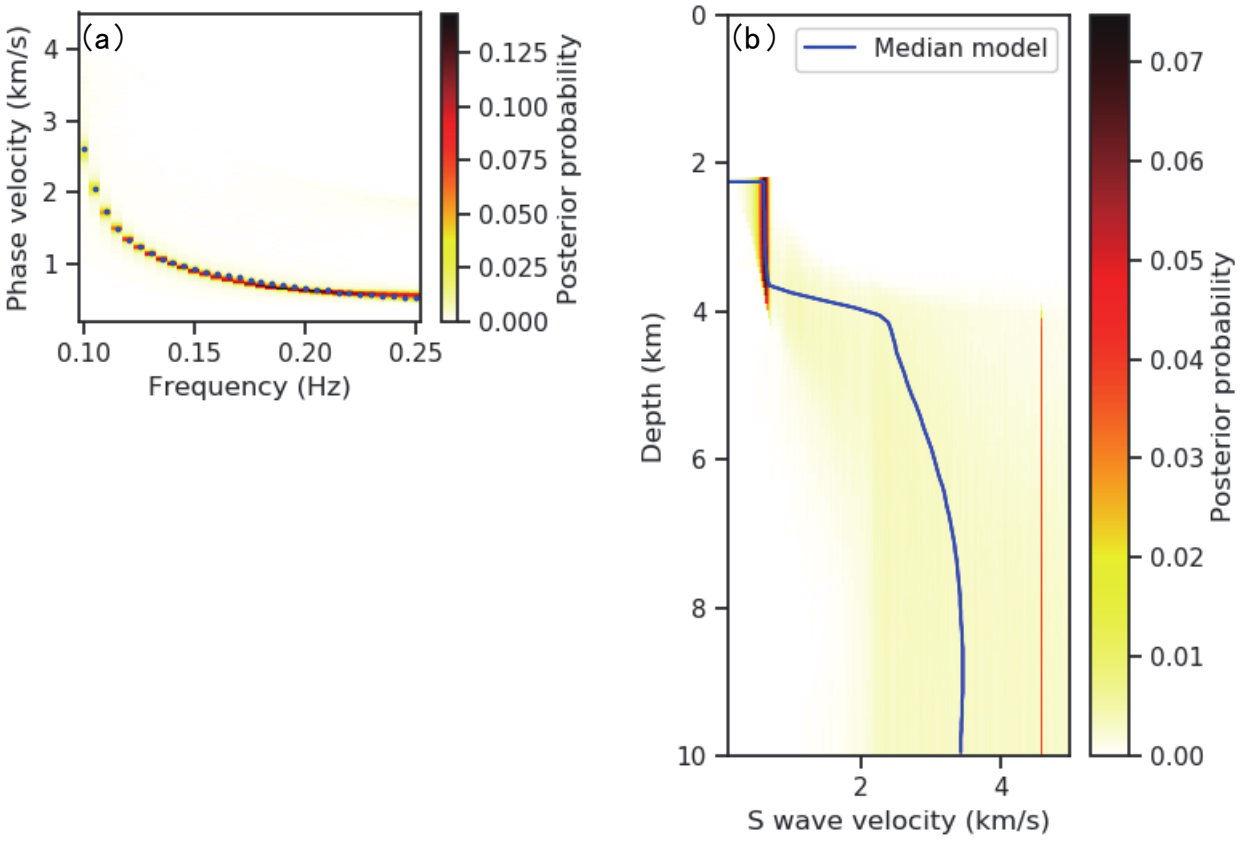

600 **Figure 10.** 1-D S-velocity structure inversion using only the fundamental mode of Rayleigh wave. The notations are the same as those in Figure 5. (a) Phase velocity of the fundamental mode of Rayleigh wave. (b) S-wave velocity structure inferred by the MCMC method.

605

610

Table 1. Search range for each station distance at the first step to measure phase-velocity perturbations. In this step, The fundamental mode first at 0.015 Hz and the first-higher mode at 0.1875 Hz are used.

Station distance	Search range for the fundamental mode	Search range for the first-higher mode
~ 10 km	-25 to 25 %	-30 to 30 %
10 ~ 15 km	-20 to 20 %	-25 to 25 %
15 ~ 20 km	-15 to 15 %	-20 to 20 %
20 km ~	-10 to 10 %	-10 to 10 %

Table 2. Search range for each station distance at the second step to measure phase-velocity perturbations. e' is the phase-velocity perturbation of the previous frequency range.

Station distance	Search range
~ 15 km	$-10 + e'$ to $10 + e'$ %
15 ~ 28 km	$-8 + e'$ to $8 + e'$ %
28 km ~	$-5 + e'$ to $5 + e'$ %